**Supporting Information**

# Integrating Multiple Regulatory Strategies: Phase, Morphology and Interface Engineering to Construct Hierarchical $Ni_2P$-$MoS_2$/rGO Heterostructure Catalyst for Efficient Oxygen Reduction Reaction

Xinyi Wang[1], Jing Jin[1], Zeyuan Gao[1], Li Hou[1,*], Xiwen Tao [1], Jing Wang[1,*], Yueqi Zhao[1] and Faming Gao[1,2,*]

[1] Hebei Key Laboratory of Applied Chemistry, State Key Laboratory of Metastable Materials Science and Technology, Yanshan University, Qinhuangdao 066004, China

[2] College of Chemical Engineering and Materials science, Tianjin University of Science and Technology, Tianjin 300457, China

* Corresponding authors.

E-mail address: holy@ysu.edu.cn; jwang6027@ysu.edu.cn; fmgao@ysu.edu.cn

# Experimental section

### Synthesis of 1T-$MoS_2$/rGO composites

The graphene oxide (GO) sheets were preliminarily synthesized by a modified Hummers' method[1]. And then, the 1T-$MoS_2$/rGO composites were prepared by a solvothermal method. The prepared GO was weighed in 20mg and added to 20mL of dispersant (NMP, DMF, $H_2O$) and ultrasonicated for 1h to obtain the graphene dispersion. 1 mmol of $(NH_4)_6Mo_7O_{24}\cdot 4H_2O$, 5 mmol of $CH_4N_2S$ and 0.1mL hydrazine hydrate ($N_2H_4\cdot H_2O$) were weighed and added to the prepared graphene dispersion, and stirred at room temperature for 30min to fully mix them. $N_2H_4\cdot H_2O$ involved as a catalyst to improve the rate of reaction and participated to split the ammonium molybdate to form intermediate compound. After it was stirred evenly, the mixture was transferred into a 50 mL Tefon-lined stainless-steel autoclave and maintained at 200°C for 24h. Eventually natural cooling to room temperature, the black suspension was put into a low-speed centrifuge and treated at 4000 rpm for 5 min. The obtained precipitates were washed by ethanol and deionized (DI) water for three times to remove impurities, and transferred to a drying oven at 60°C for 12h. The obtained sample was named 1T-$MoS_2$/rGO. The 1T-$MoS_2$ was synthesized by the same procedure as for 1T-$MoS_2$/rGO, except that no rGO was added. Then, 1T-$MoS_2$/rGO was further annealed at 350°C in the $N_2$ atmosphere with heating rate of 10 °C $min^{-1}$ and maintained at this temperature for 3 h to obtain thermodynamically stable 2H-$MoS_2$/rGO.

### Synthesis of $Ni_2P$-$MoS_2$/rGO composites

For the synthesis of $Ni_2P$-$MoS_2$/rGO composite, 50mg of the obtained 1T-$MoS_2$/rGO was dissolved in 30ml DI water, and ultrasonicated for 1h. 50mg CTAB was added to the dispersion and magnetically stirred for 15 min. Then 1mmol of $Ni(NO_3)_2\cdot 6H_2O$ and 6mmol of red phosphorus (n(Ni): n(P)=1:6) were added to the mixed solvent and strongly stirred for 1h. Moreover, the mixture was transferred into a 50 mL Tefon-lined stainless-steel autoclave and maintained at 120°C for 12h. Finally, after washing and drying, $Ni_2P$-$MoS_2$/rGO composite was obtained. According to the same above molar ratio of Ni to P and other similar steps, we also prepared $Ni_2P$-rGO and $Ni_2P$-$MoS_2$ as

comparative samples. In addition, the sample $Ni_2P$+$MoS_2$/rGO was prepared by stirring the pre-prepared 1mmol of $Ni_2P$ and $MoS_2$/rGO for 4h, and then heating the mixture at 120°C for 12h.

**Materials characterization**

The phase of samples was characterized with X-ray diffraction (XRD) analysis, which was carried out on a D/Max-2500/PC X-ray diffractometer with Cu Kα radiation (λ=1.5418Å 2θ=5 to 85°). The morphology was recorded via Field emission scanning electron microscopy (FE-SEM, S4800, Hitachi) with elementary disperse spectroscope (EDS) mapping analysis. Transmission electron microscopy and High-resolution transmission electron microscopy with a field emission gun operating at 200 kV was investigated by FEI Tecnai F30. The valence states and bond structure of the samples were analyzed comprehensively by X-ray photoelectron spectroscopy (XPS) (ThermoFischer ESCALAB 250Xi), and all the binding energies were standardized by C 1s peak energy at 284.6 eV. Renishaw micro-Raman spectrometer (λ=514 nm) was used to study Raman scattering. Raman spectra were recorded on Renishaw micro-Raman spectrometer equipped with Ar laser (wavelength=514 nm). In addition, nitrogen physisorption at 77 K on a Micromeritics V-Sorb 2800 P analyzer was carried out to obtain Nitrogen adsorption and desorption isotherms. Fourier-Transform Infrared Spectrometer (FT-IR) spectroscopy analysis was conducted by VERTEX 70. The surface wettability of the samples was carried out by assessing the water contact angles. In this work, a 2μL electrolyte was dropped on the catalytic electrode.

**Electrochemical measurement**

The electrochemical performance of the prepared catalyst was recorded on CHI 760E electrochemical workstation combining with rotating disk electrode (RDE, 5 mm in diameter). The test system is a traditional three-electrode system, including a RDE coated with catalyst ink was used as a working electrode, a Pt sheet as a counter electrode, and an Ag/AgCl electrode as a reference electrode and 0.1 M KOH aqueous solution as the electrolyte. All potentials in the experiment were converted to relative hydrogen electrode as standard potential (RHE) according to the formula

$E_{RHE} = E_{Ag/AgCl} + 0.0592pH + E^{\theta}_{Ag/AgCl}$.The preparation method of working electrode ink was as follows: 5 mg sample was put into 3 mL glass hydrophobic vial, and then added 970μL of ethanol solution (V(water):V(absolute ethanol)=3:1) and 30μL of Nafion solution (5 wt%), sonicated for 40 min until a black uniform suspension was obtained. 10μL ink is absorbed by the pipette gun, then slowly dropped on the treated glassy carbon electrode, and dried under natural conditions.

Cyclic voltammetry (CV) test is to control the electrode potential to change at a constant rate within a certain potential range, different reduction and oxidation reactions occur alternately on the electrode, and record the curve of the response current changing with the potential. In this experiment, the CV test is carried out in 0.1M KOH electrolyte saturated with $N_2$ at a certain scanning rate within the range of 0-1V potential. Its main function is to activate the catalyst so that the subsequent test can be faster and more accurate; Linear sweep voltammetry (LSV) is a current potential curve obtained by linear potential scanning at a constant scanning rate within a certain potential range and collecting response currents under different potentials. In this experiment, the LSV test was accomplished in 0.1M KOH electrolyte saturated with $O_2$. The rotation speed of the RDE was kept at 1600 rpm, and linear scanning was carried out at a scanning rate of 5mV/s within the range of 0-1V potential. The onset potential ($E_{onset}$), half-wave potential ($E_{1/2}$) and Tafel slope can be obtained from the LSV, which are key indicators for evaluating the electrocatalytic performance of the material; To further determine the number of transferred electrons per $O_2$, the rotational speed of the RDE was adjusted to vary from 400 to 2000 rpm. The number of transferred electrons is calculated by the Koutecky-Levich equation (K-L equation); The electrochemical impedance (EIS) study was carried out in a frequency range of $10^6$ Hz to $10^{-2}$ Hz with an AC amplitude of 5 mV under the open circuit voltage conditions; Long cycle test was used to characterize the stability of the catalyst.

**Computational methods**

The density functional theory (DFT) calculations were performed by Vienna Ab initio Simulation Package (VASP) with the projector-augmented plane wave (PAW)

approach[2]. In the calculations, the generalized gradient approximation (GGA) was treated using the Perdew-Burke-Ernzerhof (PBE) exchange-correlation functional[3]. The cut-off energy of the plane-wave basis was set to 500 eV for calculations of atoms and cell optimization. All the resulting slab models were separated by an ≈20 Å vacuum gap with 3 × 3 × 1 k-point mesh[4]. The heterogeneous interface model was built from the (111) facet of $Ni_2P$ and the (002) facet of $MoS_2$ monolayer. All the atom positions in the model were optimized by the conjugate-gradient optimization procedure. During the calculations, the free energy changes of the four steps for ORR were investigated：

$$O_2 + {}^* + e^- + H_2O \rightarrow OOH^* + OH^- \qquad \Delta G_I \tag{1}$$

$$OOH^* + e^- \rightarrow O^* + OH^- \qquad \Delta G_{II} \tag{2}$$

$$O^* + e^- + H_2O \rightarrow OH^* + OH^- \qquad \Delta G_{III} \tag{3}$$

$$OH^* + e^- \rightarrow OH^- \qquad \Delta G_{IV} \tag{4}$$

where * represents an active site on the surface, $\Delta G_I$, $\Delta G_{II}$, $\Delta G_{III}$ and $\Delta G_{IV}$, represent the free energies of adsorption for the above four elementary steps. The calculating formula of the free energy is as follows:

$$\Delta G=\Delta E_{DFT}+\Delta E_{ZPE}-T\Delta S$$

Where $\Delta G$ is the free energy changes of each step, $\Delta E_{DFT}$ is the adsorption energy of adsorbed species on the given unit cell, $\Delta E_{ZPE}$ and $T\Delta S$ are the zero-point energy and entropy difference of the adsorbate[5]. The overpotential in ORR is calculated as follows:

$$\eta_{ORR} = 1.23\text{-min } \{\Delta G_I, \Delta G_{II}, \Delta G_{III}, \Delta G_{IV}\}/e$$

# Supplementary figures:

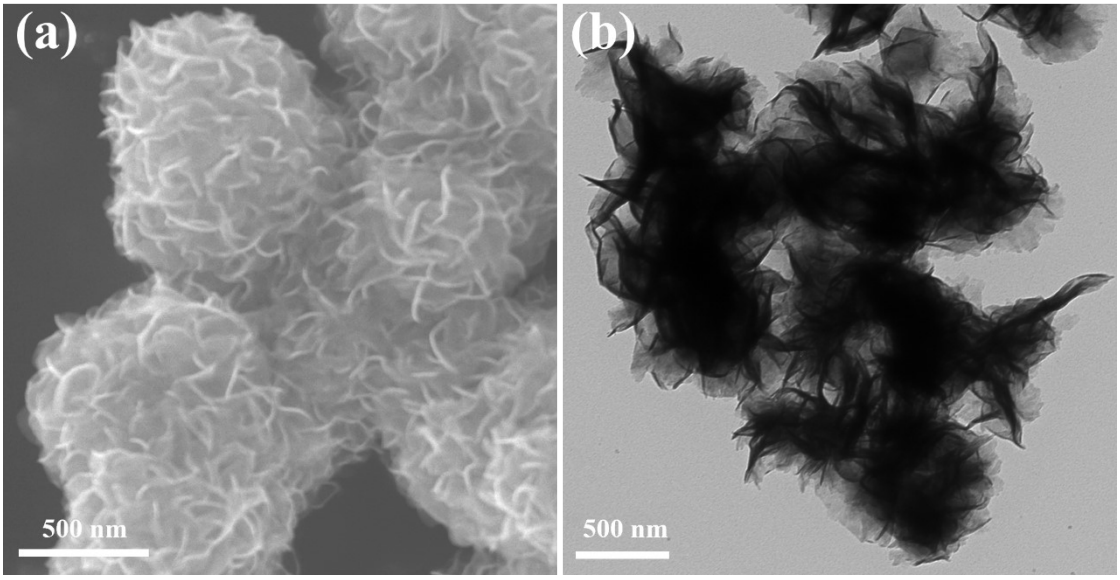


**Fig. S1.** (a) SEM and (b) TEM images of the bare 1T-$MoS_2$.

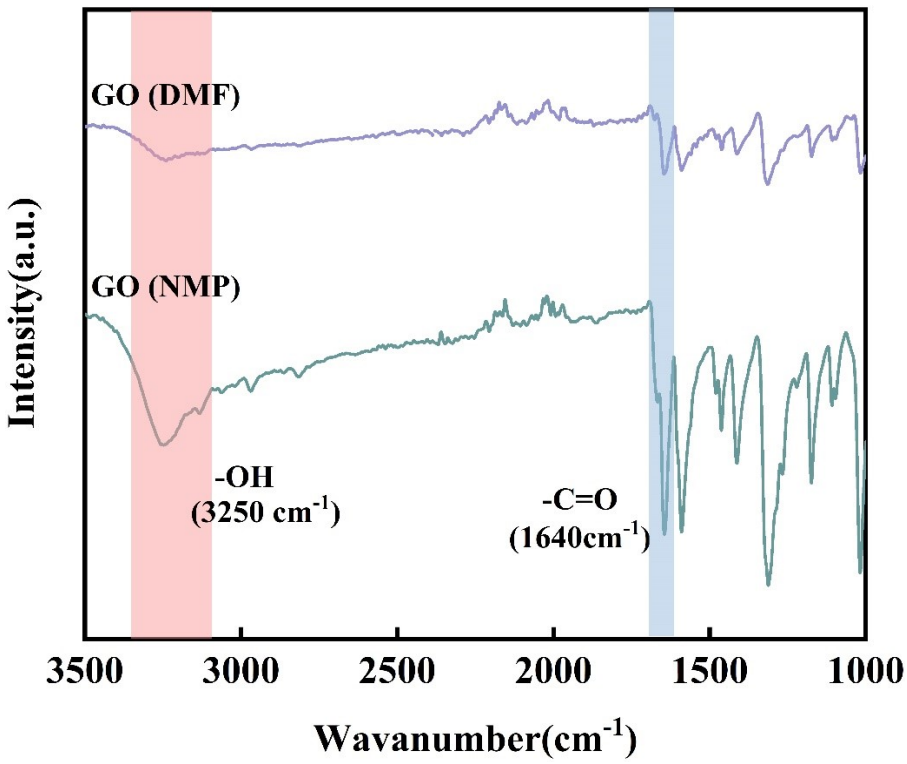


**Fig. S2.** FTIR spectra of the GO (DMF) and GO (NMP).

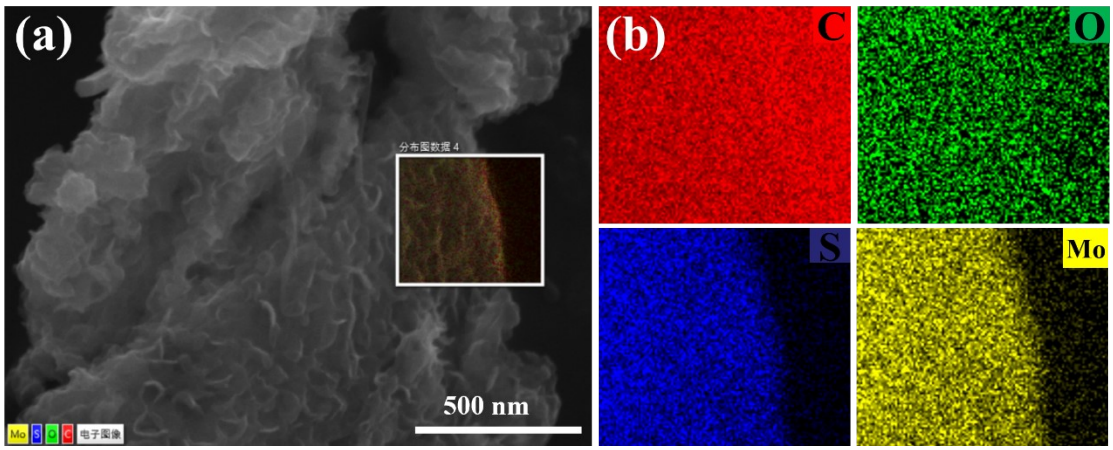


**Fig. S3**. SEM-EDS mapping of 1T-$MoS_2$/rGO (DMF).

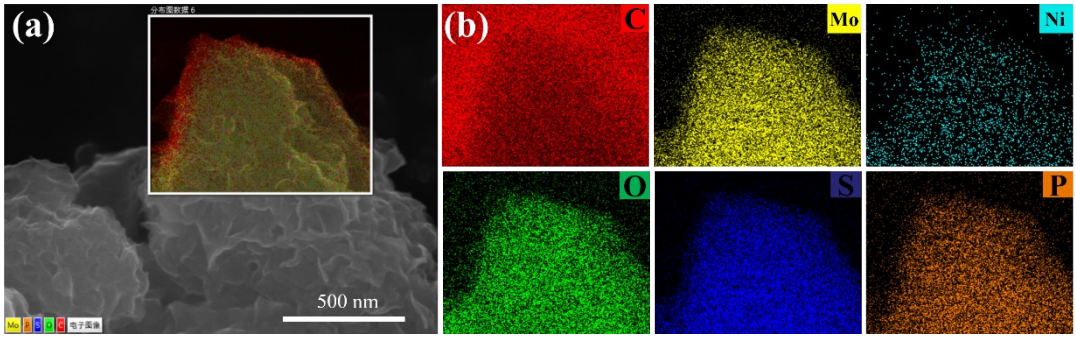


**Fig. S4.** SEM-EDS mapping of $Ni_2P$-$MoS_2$/rGO

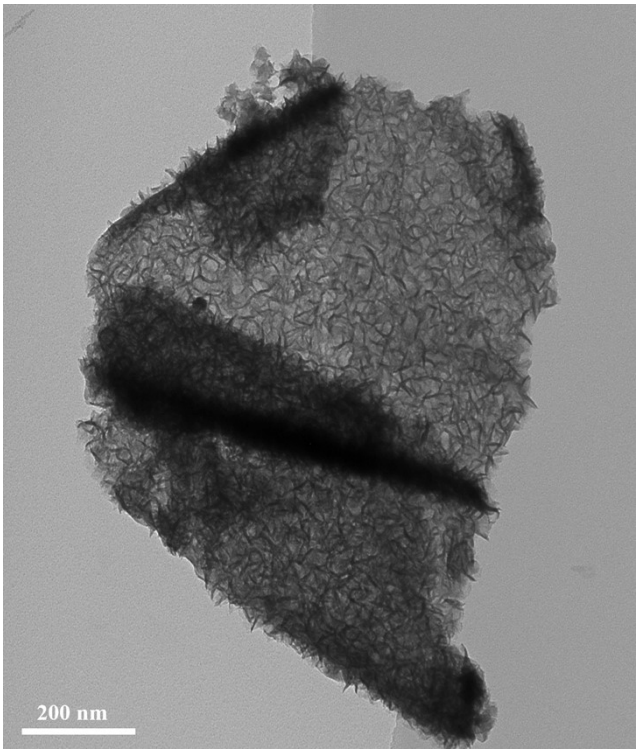


**Fig. S5.** TEM image of 2H-$MoS_2$/rGO.

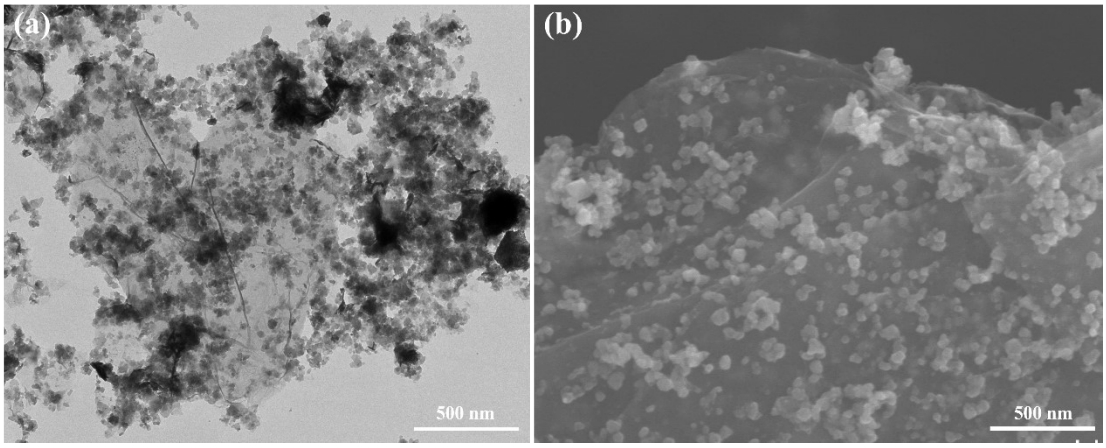


**Fig. S6.** (a) TEM and (b) SEN images of $Ni_2P$-rGO.

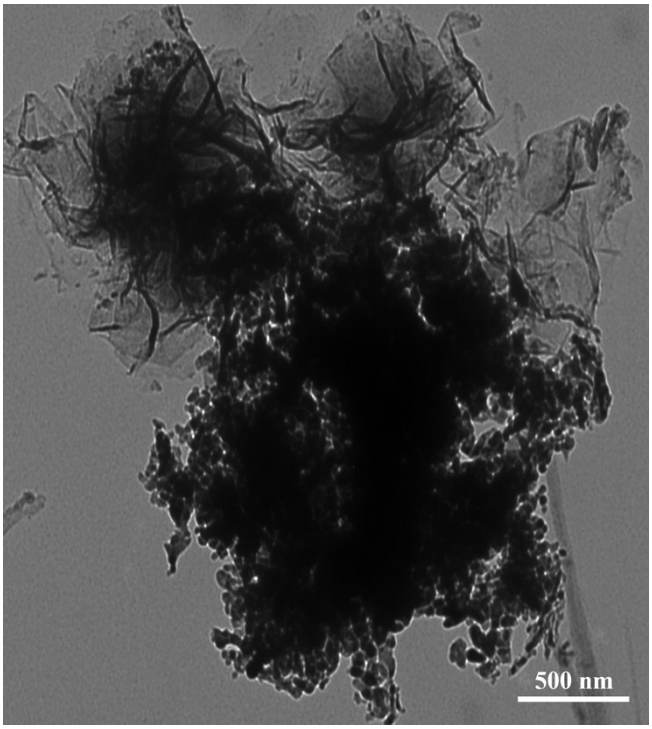


**Fig. S7.** TEM image of $Ni_2P$+$MoS_2$/rGO.

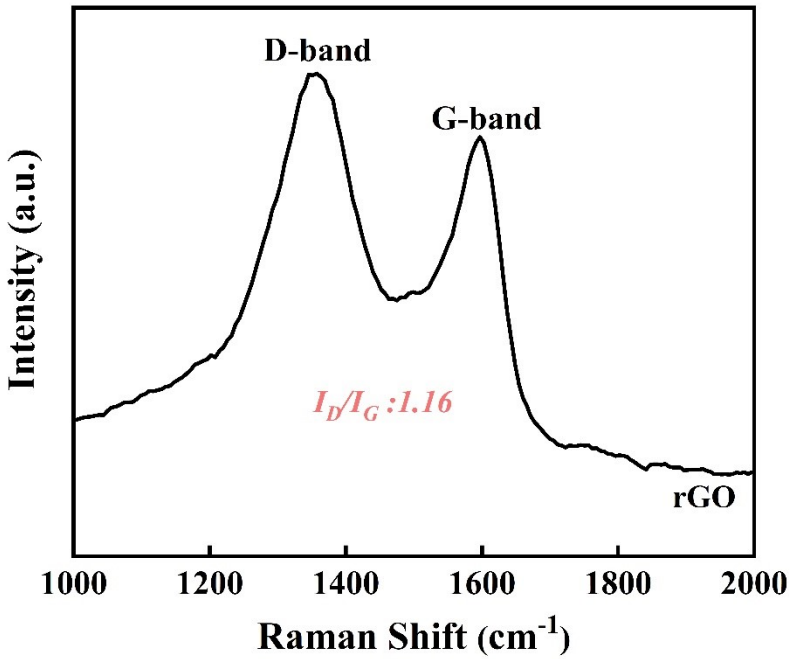


**Fig. S8.** Raman spectra of rGO.

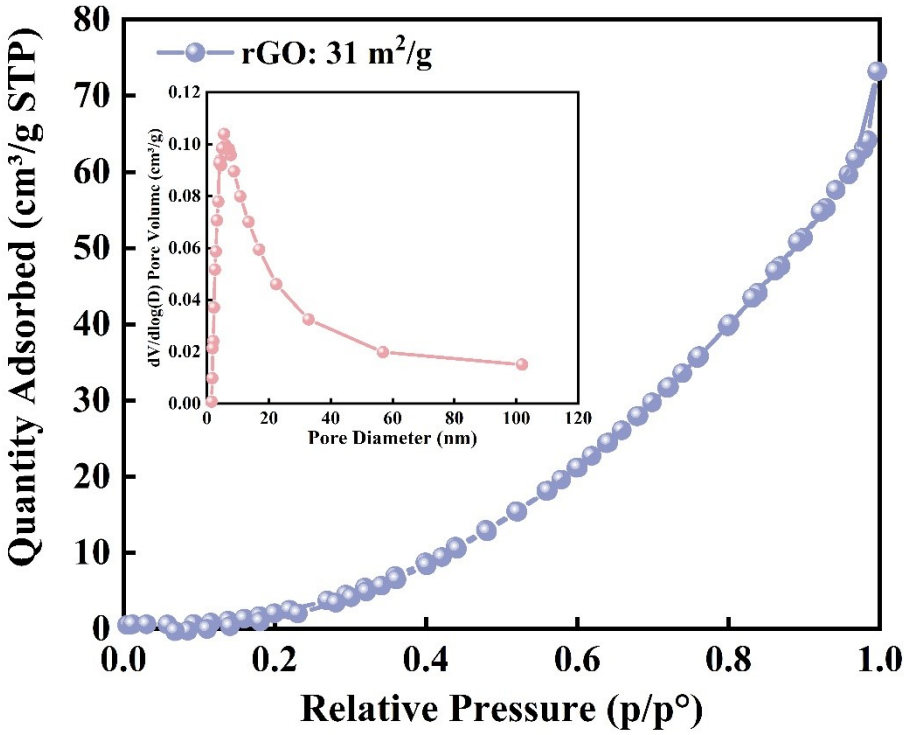


**Fig. S9.** $N_2$ adsorption-desorption isotherm of rGO, and the corresponding pore size distribution curve (inset).

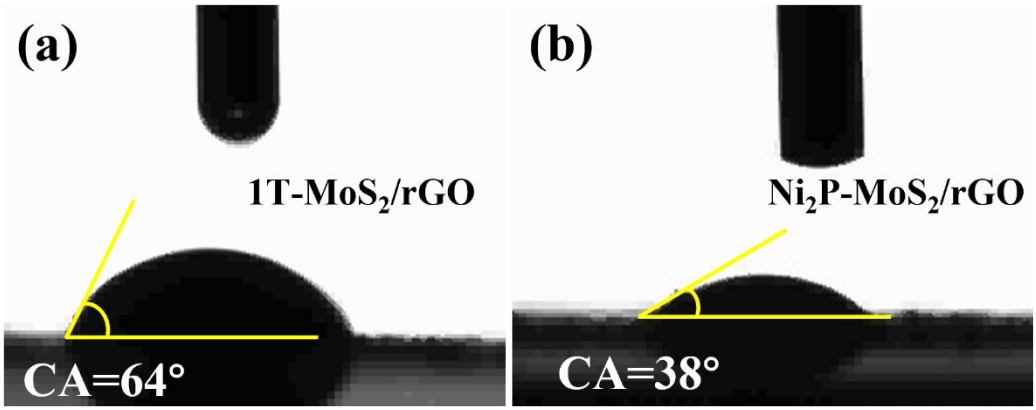


**Fig. S10.** Water contact angle of (a) 1T-$MoS_2$/rGO and (b) $Ni_2P$-$MoS_2$/rGO.

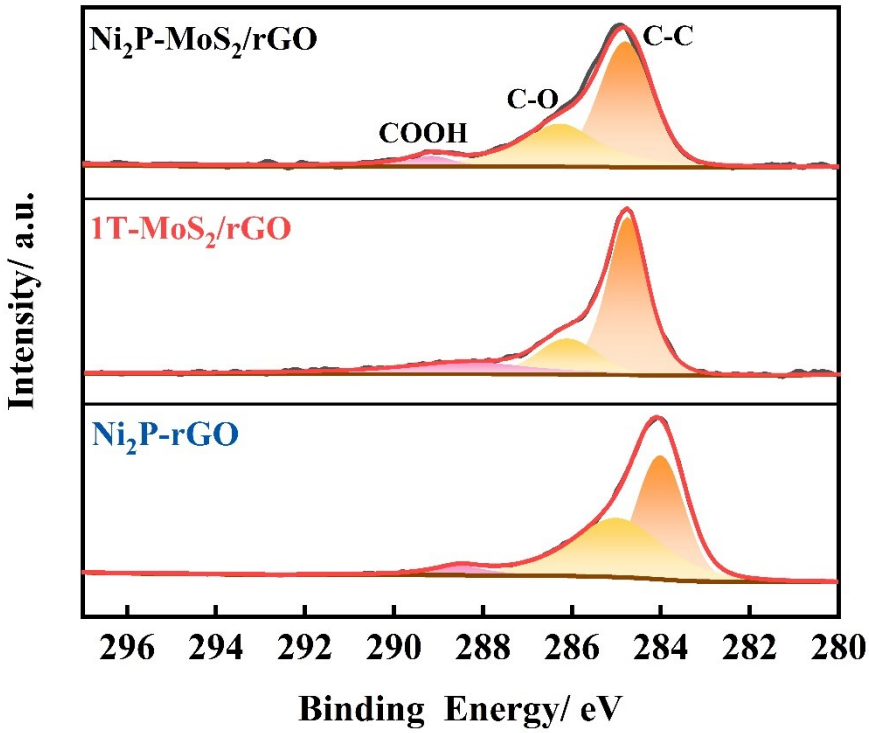


**Fig. S11.** XPS profiles of C 1s of $Ni_2P$-$MoS_2$/rGO, 1T-$MoS_2$/rGO and $Ni_2P$-rGO samples.

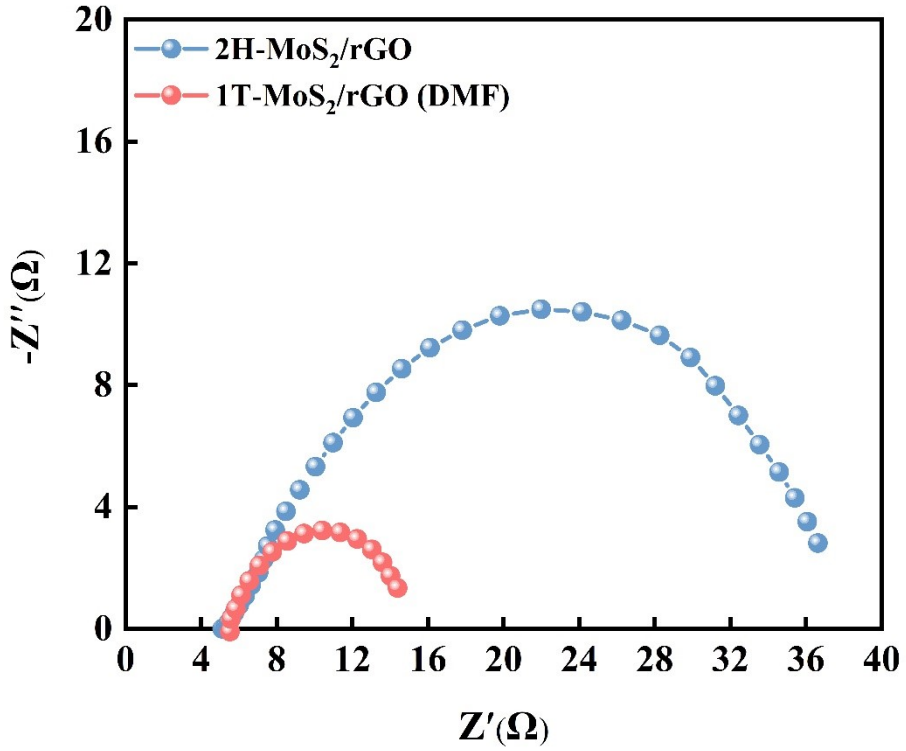


**Fig. S12.** Nyquist plots of 2H-$MoS_2$/rGO and 1T-$MoS_2$/rGO.

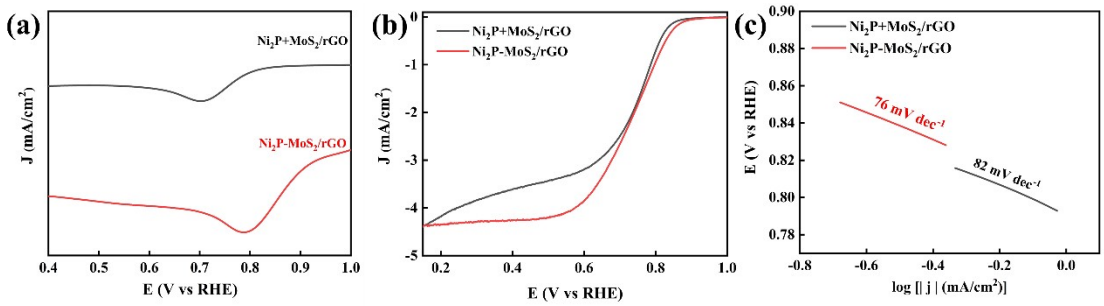


**Fig. S13.** (a) CV curves; (b) LSV curves; (c) Tafel slope of $Ni_2P$+$MoS_2$/rGO and $Ni_2P$-$MoS_2$/rGO.

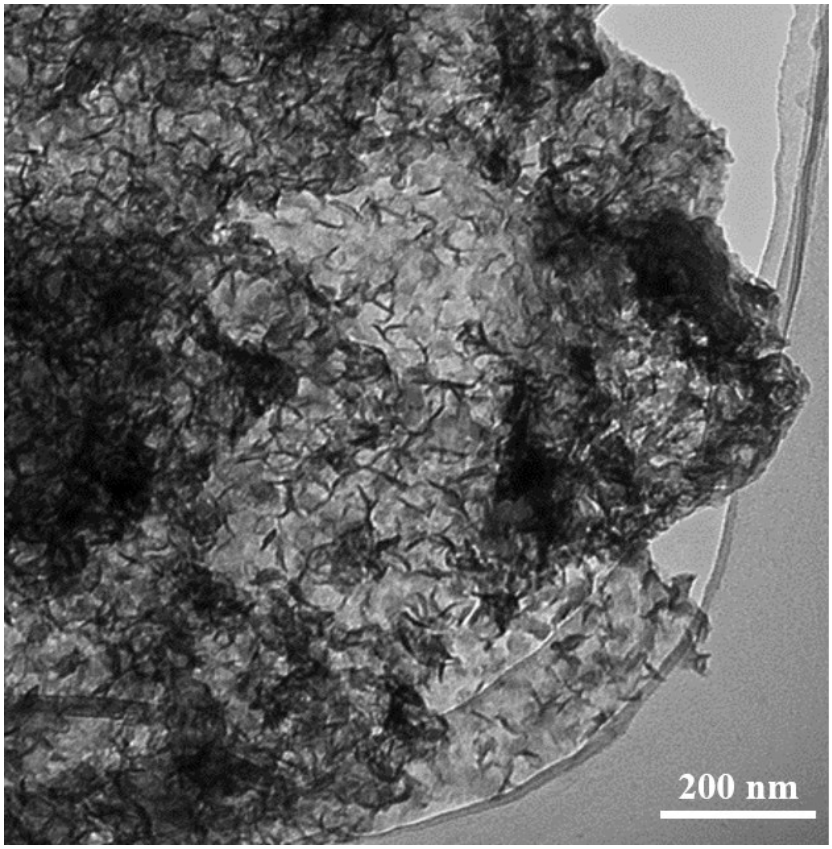


**Fig. S14.** TEM image of 1T-$MoS_2$/rGO (DMF) after long-term ORR tests.

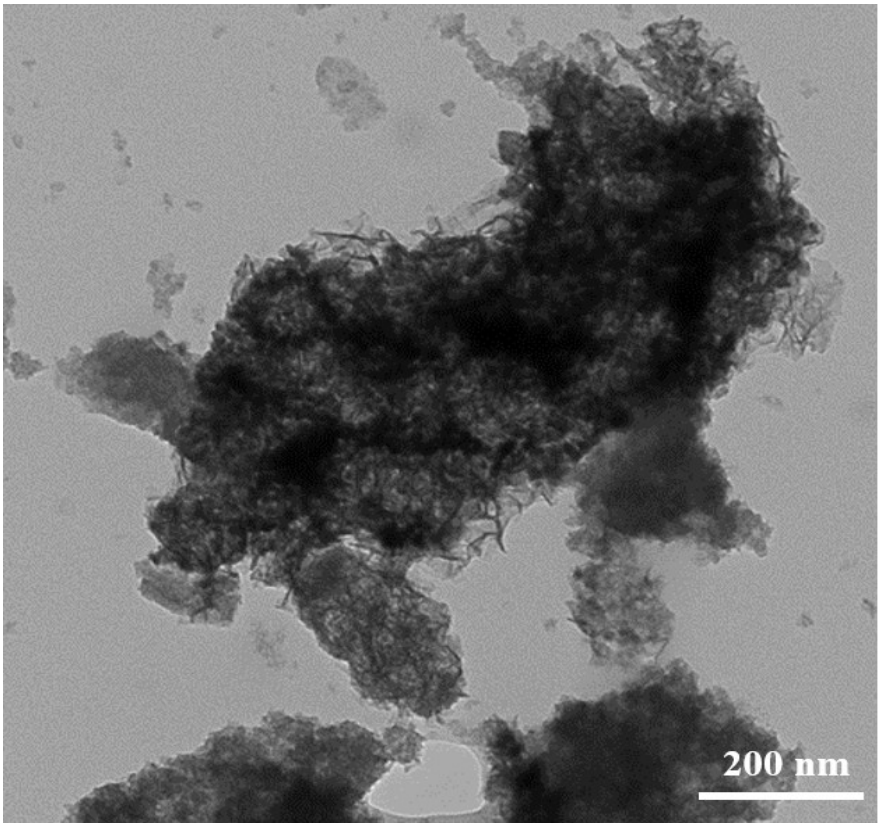


**Fig. S15.** TEM image of $Ni_2P$-$MoS_2$/rGO after long-term ORR tests

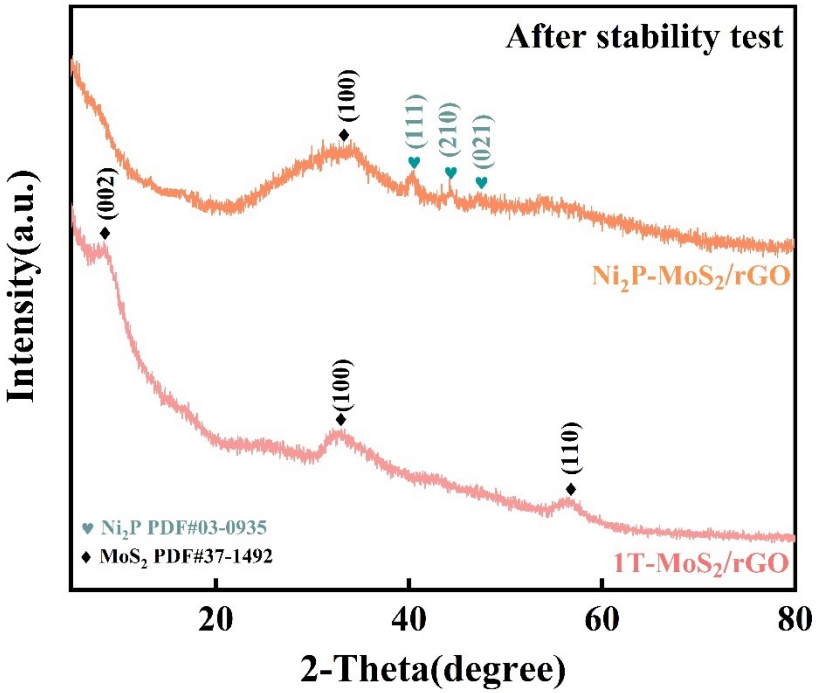


**Fig. S16.** XRD patterns of 1T-$MoS_2$/rGO and $Ni_2P$-$MoS_2$/rGO after stability test.

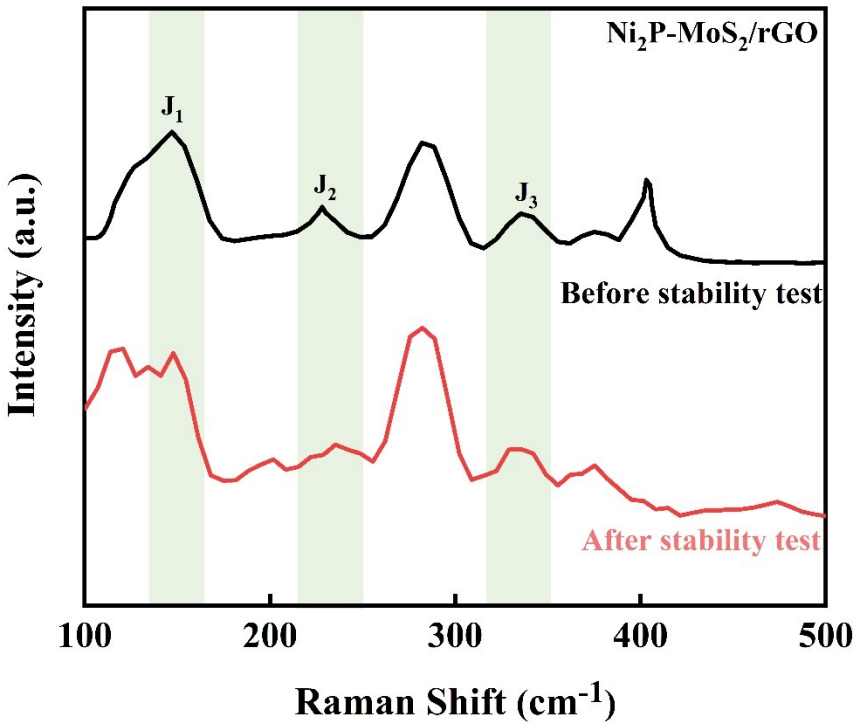


**Fig. S17.** Raman spectra of $Ni_2P$-$MoS_2$/rGO before and after stability test.

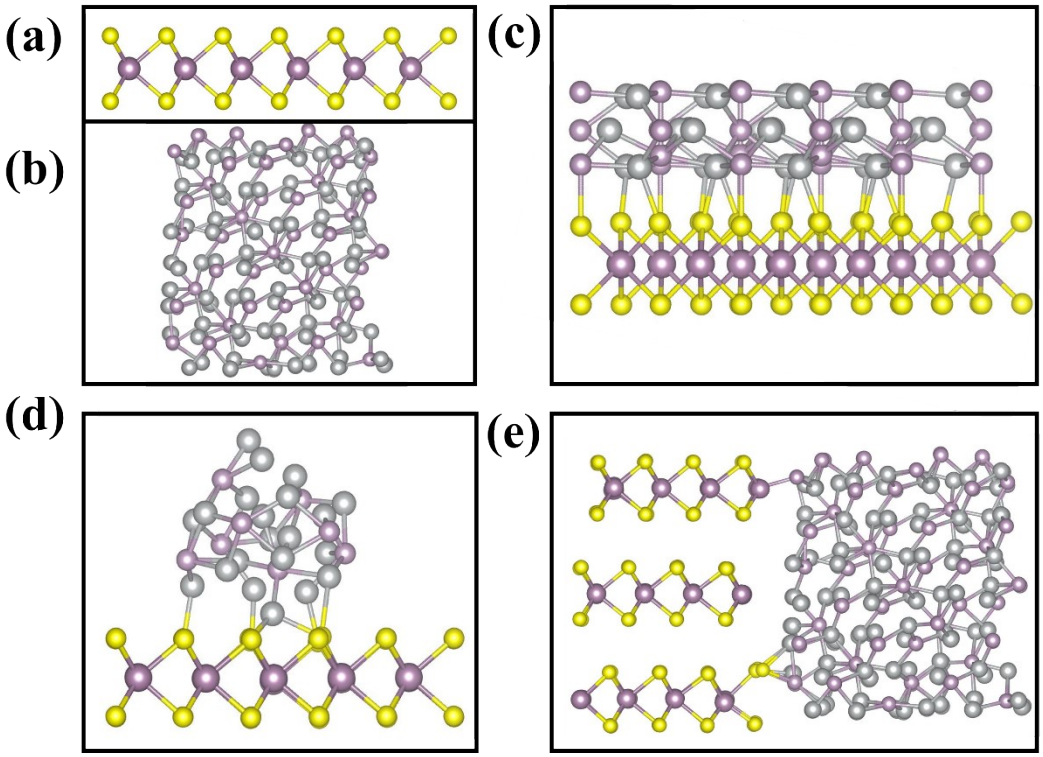


**Fig. S18.** The structural modes of (a) $MoS_2$, (b) $Ni_2P$, (c) layer structured $Ni_2P$-$MoS_2$, (d) cluster structured $Ni_2P$-$MoS_2$, (e) hetero-structured $Ni_2P$-$MoS_2$.

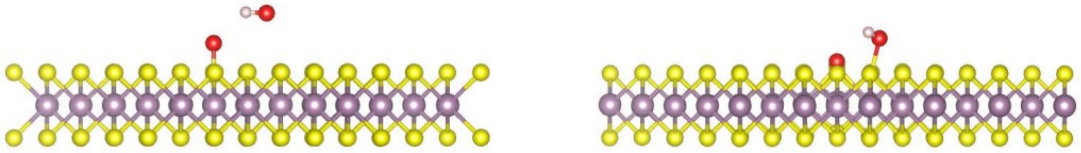

**Fig. S19.** Atomistic structure of optimized configuration for *OOH adsorption on the (002) plane of $MoS_2$.

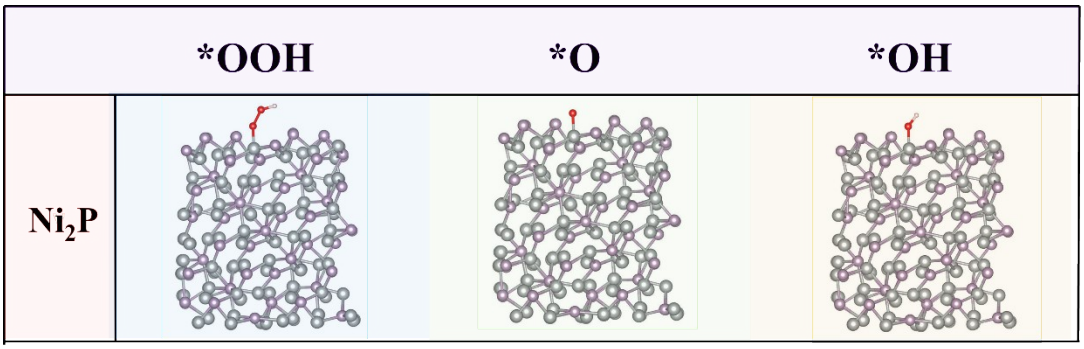


**Fig. S20.** Atomistic structure of optimized configuration for the (111) plane $Ni_2P$.

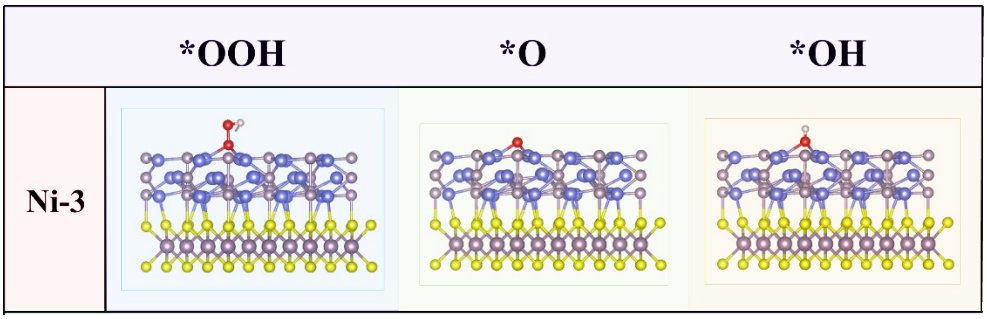


**Fig. S21.** Atomistic structure of optimized configuration for *OOH, *O, *OH intermediates adsorption on Ni-3 of layer structure $Ni_2P$-$MoS_2$.

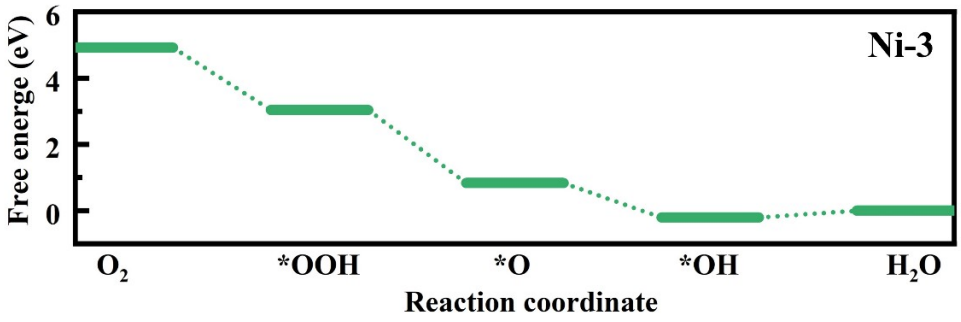


**Fig. S22.** Gibbs free energy diagram for the four steps of ORR for layer structure $Ni_2P$-$MoS_2$ on Ni-3. $Ni_2P$-$MoS_2$ (Ni-3) exhibits intense binding for *OH intermediate, resulting in difficult desorption.

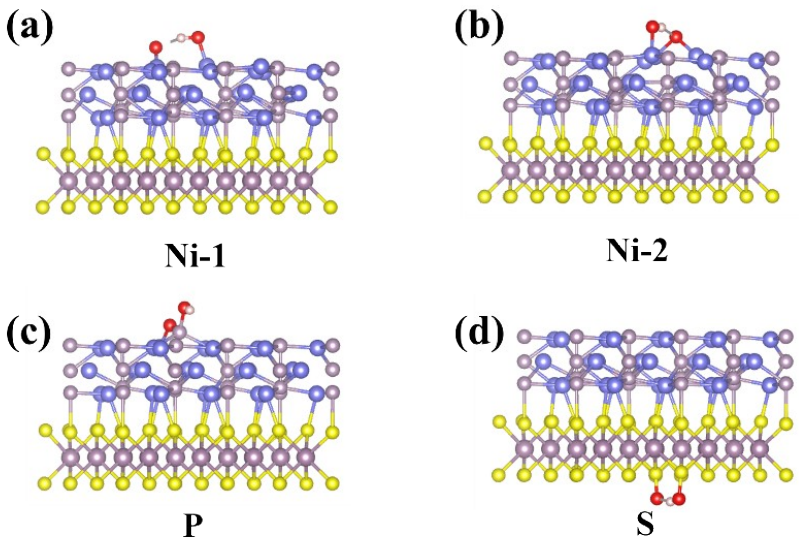


**Fig. S23.** Atomistic structure of optimized configuration for *OOH adsorption on other sites of layer structure $Ni_2P$-$MoS_2$. (a) Ni-1, (b) Ni-2, (c) P and (d) S, respectively. However, in the further theoretical calculation, the intermediates decomposition or extremely difficult to adsorb, resulting in no catalytic activity on other sites.

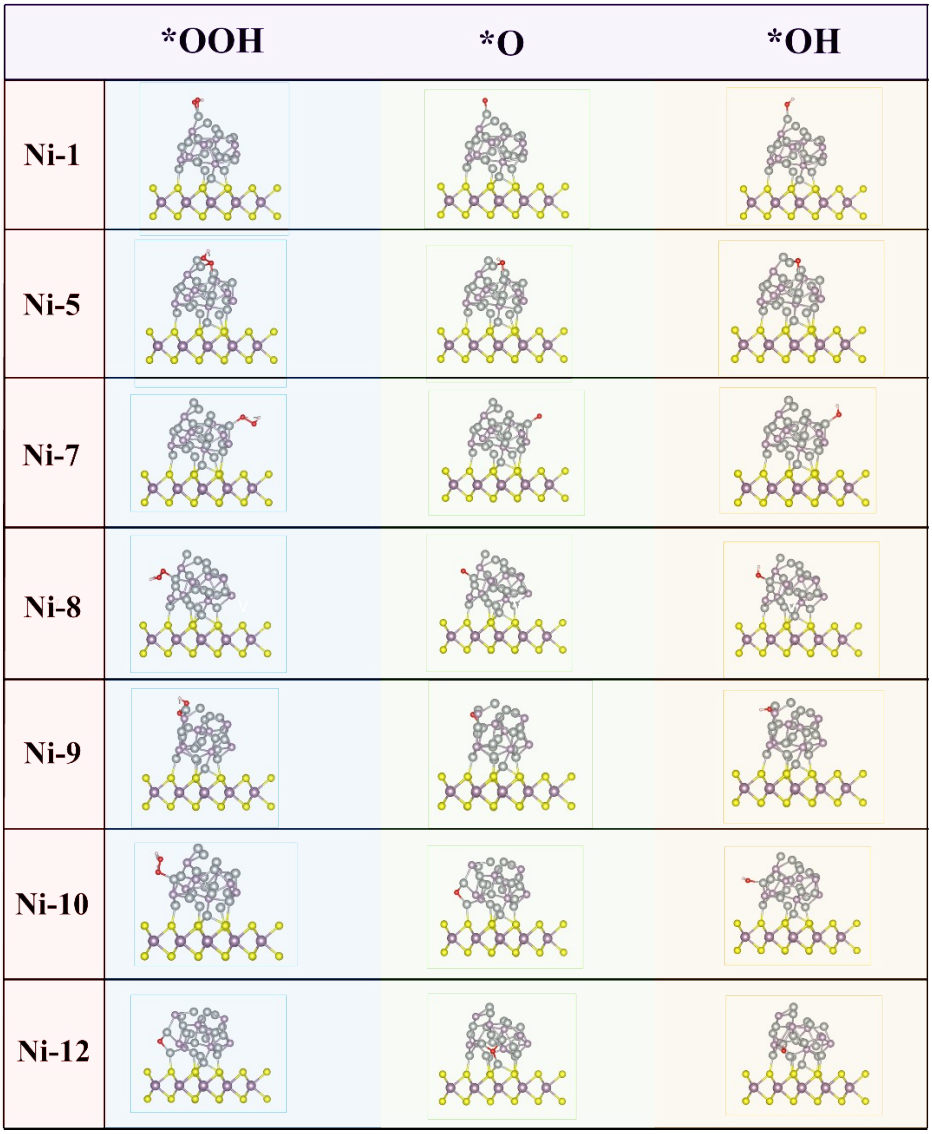


**Fig. S24.** Atomistic structure of optimized configuration for *OOH, *O, *OH intermediates on different adsorption sites of cluster structure $Ni_2P$-$MoS_2$ (Ni-1, 5, 7, 8, 9, 10 and 12).

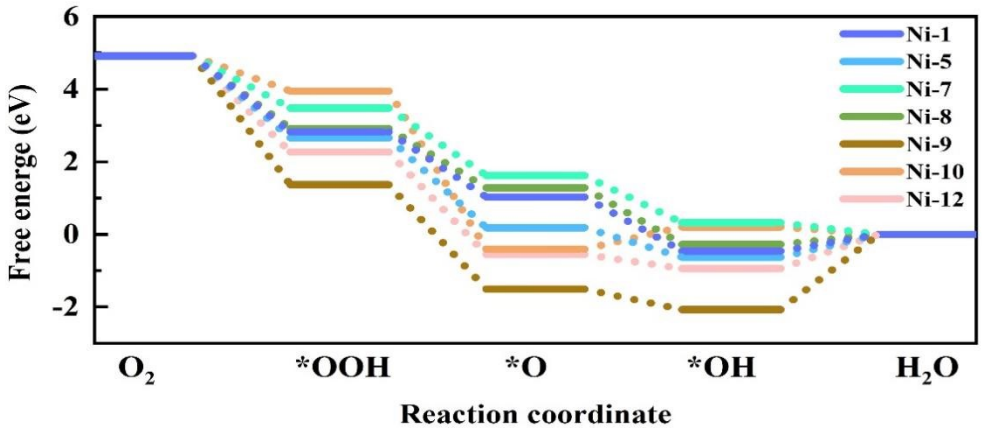


**Fig. S25.** Gibbs free energy diagram for the four steps of ORR for cluster structure $Ni_2P$-$MoS_2$ on different adsorption sites (Ni-1, 5, 7, 8, 9, 10 and 12). The overpotential of $Ni_2P$-$MoS_2$ is 0.91 V on Ni-7, and on Ni-1, 5, 8, 9, 10 and 12 exhibits strong adsorption on oxygen containing intermediates.

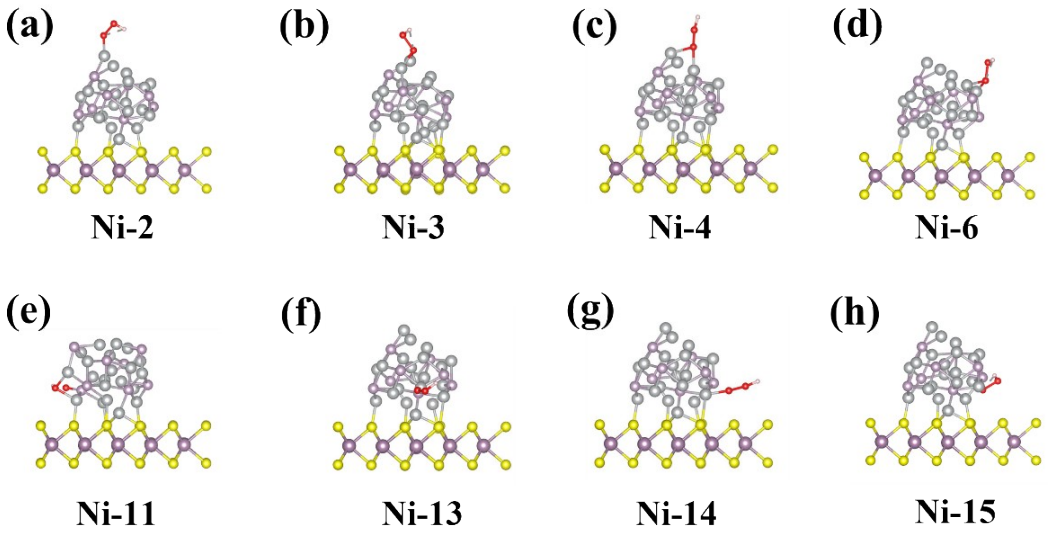


**Fig. S26.** Atomistic structure of optimized configuration for *OOH adsorption on other sites of cluster structure $Ni_2P$-$MoS_2$. However, in the further theoretical calculation, the intermediates decomposition or extremely difficult to adsorb, resulting in no catalytic activity on other sites.

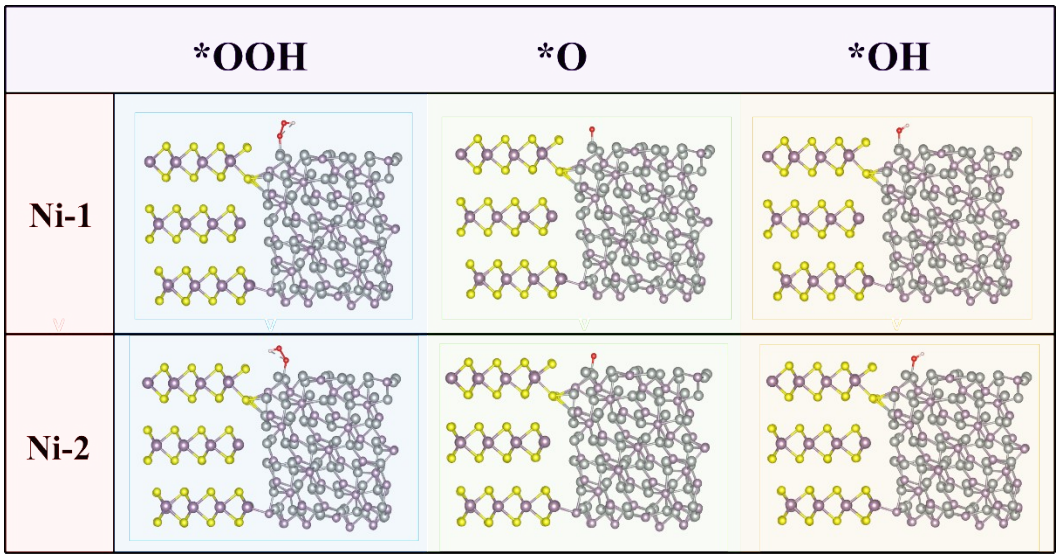


**Fig. S27.** Atomistic structure of optimized configuration for *OOH, *O, *OH intermediates adsorption on Ni-1 and 2 of heterostructure $Ni_2P$-$MoS_2$.

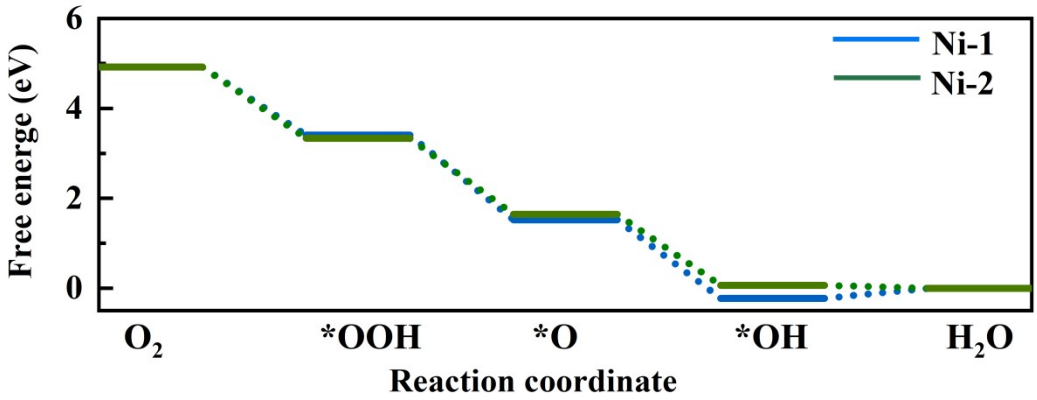


**Fig. S28.** Gibbs free energy diagram for the four steps of ORR for cluster structure $Ni_2P$-$MoS_2$ on Ni-1 and 2. The overpotential of $Ni_2P$-$MoS_2$ is as high as 1.63 V on Ni-1, and $Ni_2P$-$MoS_2$ (Ni-2) display intense binding for *OH intermediate.

**Table S1.** Comparison of ORR performances for $Ni_2P$-$MoS_2$/rGO composite catalyst with previously reported $MoS_2$-based electrocatalysts in the alkaline media.

| Catalysts | $E_{onset}$ (V vs. RHE) | $E_{1/2}$ (V vs. RHE) | *Tafel slope* (mV/dec) | Electron transfer number | *Refs.* |
|---|---|---|---|---|---|
| $Ni_2P$-$MoS_2$/rGO | 0.916 | 0.732 | 80 | 4.115 | This work |
| N-GQDs/$MoS_2$-rGO | 0.81 | About 0.6 | _ _ | 3.2-2.8 | 6 |
| $Ni_3S_2$/$MoS_2$ | 0.95 | 0.885 | 67.54 | 4.0-4.1 | 7 |
| $MoS_2$-rGO | 0.8 | _ _ | _ _ | 3-3.32 | 8 |
| 1T-$MoS_2$/CNT | 0.94 | 0.81 | _ _ | 3.79-3.83 | 9 |
| G@N-$MoS_2$ | 0.82 | About 0.7 | _ _ | _ _ | 10 |
| CoOx/mC@$MoS_2$@g-$C_3N_4$ | 0.89 | About 0.7 | 84 | 3.5-3.8 | 11 |
| $Mo_2C$-$MoS_2$ | _ _ | 0.6 | _ _ | 3.72 | 12 |
| $Co(OH)_2$-$MoS_2$/rGO | 0.855 | 0.731 | 63 | 3.2-3.6 | 13 |
| $NiFe_2O_4$/$MoS_2$ | 0.82 | _ _ | _ _ | 3.2 | 14 |
| NC@$MoS_2$@Co-Fe | 0.84 | 0.73 | 60 | _ _ | 15 |
| CuS@$MoS_2$ | 0.87 | 0.76 | _ _ | 3.95 | 16 |

## Notes and references


1 D. C. Marcano, D. V. Kosynkin, J. M. Berlin, A. Sinitskii, Z. Z. Sun, A. Slesarev, L. B. Alemany, W. Lu, J. M, Tour. Improved synthesis of graphene oxide, *ACS Nano*, 2010, **4**, 4806-4814.

2 J. P. Perdew, K. Burke, M. Ernzerhof, Generalized gradient approximation made simple, *Phys. Rev. Lett.*, 1996, **77**, 3865-3868.

3 G. Kresse, D. Joubert, From ultrasoft pseudopotentials to the projector augmented-wave method, *Phys. Rev. B*, 1999, **59**, 1758-1775.

4 H. J. Monkhorst, J. D. Pack, Special points for brillouin-zone integrations, *Phys. Rev. B*, 1976, **13**, 1746-1747.

5 F. Liu, L. Shi, S. Song, K. Ge, X. Zhang, Y. Guo, D. Liu, Simultaneously engineering the coordination environment and pore architecture of metal-organic framework-derived single-atomic iron catalysts for ultraefficient oxygen reduction, *Small*, 2021, **17**, 2102425.

6 R. Vinoth, I. M. Patil, A. Pandikumar, B. A. Kakade, N. M. Huang, D. D. Dionysios, B. Neppolian, Synergistically enhanced electrocatalytic performance of an N-doped graphene quantum dot-decorated 3D $MoS_2$-graphene nanohybrid for oxygen reduction reaction, *ACS Omega*, 2016, **1**, 971-980.

7 J. Mao, P. Liu, C. Du, D. Liang, J. Yan, W. Song, Tailoring 2D $MoS_2$ heterointerfaces for promising oxygen reduction reaction electrocatalysis, *J. Mater. Chem. A*, 2019, **7**, 8785-8789.

8 J. Zhou, H. Xiao, B. Zhou, F. Huang, S. Zhou, W. Xiao, D. Wang, Hierarchical $MoS_2$-rGO nanosheets with high $MoS_2$ loading with enhanced electro-catalytic performance, *Appl. Surf. Sci.*, 2015, **358**, 152-158.

9 Z. Sadighi, J. Liu, L. Zhao, F. Ciucci, J. K. Kim, Metallic $MoS_2$ nanosheets: multifunctional electrocatalyst for the ORR, OER and Li-$O_2$ batteries, *Nanoscale*, 2018, **10**, 22549-22559.

10 C. Du, H. Huang, X. Feng, S. Wu, W. Song, Confining $MoS_2$ nanodots in 3D porous nitrogen-doped graphene with amendable ORR performance, *J. Mater. Chem. A*, 2015, **3**, 7616-7622.

11 L. He, B. Cui, J. Liu, M. Wang, Z. Zhang, H. Zhang, Fabrication of porous $CoO_x$/mC@$MoS_2$ composite loaded on g-$C_3N_4$ nanosheets as a highly efficient dual electrocatalyst for oxygen reduction and hydrogen evolution reactions, *ACS Sustainable Chem. Eng.*, 2018, **6**, 9257-9268.

12 A. P. Tiwari, Y. Yoon, T. G. Novak, A. Azam, M. Lee, S. S. Lee, G. H. Lee, D. J. Srolovitz, K. S. An, S. Jeon, Lattice strain formation through spin-coupled shells of $MoS_2$ on $Mo_2C$ for bifunctional oxygen reduction and oxygen evolution reaction electrocatalysts, *Adv. Mater. Interfaces*, 2019, **6**, 1900948.

13 R. Illathvalappil, S. M. Unni, S. Kurungot, Layer-separated $MoS_2$ bearing reduced graphene oxide formed by an in situ intercalation-cum-anchoring route mediated by $Co(OH)_2$ as a Pt-free electrocatalyst for oxygen reduction, *Nanoscale*, 2015, **7**, 16729-16736.

14 M. M. Sebastian, P. Velayudham, A. Schechter, N. Kalarikkal, Spinel nickel ferrite nanoparticles supported on a 1T/2H mixed-phase $MoS_2$ heterostructured composite as a bifunctional electrocatalyst for oxygen evolution and oxygen reduction reactions, *Energy Fuels*, 2022, **36**, 7782-7794.

15 X. Shang, Q. Shen, Y. Xiong, Z. Jiang, C. Qin, X. Tian, X. Yang, Z. Jiang, Effect of Co-Fe alloy nanoparticles on the surface electronic structure of molybdenum disulfide nanosheets and its application as a bifunctional catalyst for rechargeable zinc air battery, *J. Alloys Compd.*, 2022, **916**, 165482.

16 Avraham Bar-Hen, Ronen Bar-Ziv, Tsion Ohaion-Raz, Amir Mizrahi, Simon Hettler, Raul Arenal, Maya Bar Sadan, Shelling with $MoS_2$: Functional CuS@$MoS_2$ hybrids as electrocatalysts for the oxygen reduction and hydrogen evolution reactions, *Chem. Eng. J*, 2021, **420**, 129771.